



Refractive index sensing using quasi-bound states in the continuum in silicon metasurfaces

TOM VAN LOON,¹  MINPENG LIANG,^{1,4}  THOMAS DELPLACE,²
BJORN MAES,²  SHUNSUKE MURAI,³ PETER ZIJLSTRA,¹  AND
JAIME GÓMEZ RIVAS^{1,5} 

¹Department of Applied Physics and Science Education, Institute for Complex Molecular Systems, and Eindhoven Hendrik Casimir Institute, PO Box 513, Eindhoven 5600 MB, The Netherlands

²Micro- and Nanophotonic Materials Group, Research Institute for Materials Science and Engineering, University of Mons, 20 Place du Parc, Mons B-7000, Belgium

³Department of Material Chemistry, Graduate School of Engineering, Kyoto University, Nishikyo-ku, Kyoto 615-8510, Japan

⁴m.liang1@tue.nl

⁵J.Gomez.Rivas@tue.nl

Abstract: This work presents a bulk refractive index sensor based on quasi-bound states in the continuum (BICs) induced by broken symmetries in metasurfaces. The symmetry is broken by detuning the size and position of silicon particles periodically arranged in an array, resulting in multiple quasi-BIC resonances. We investigate the sensing characteristics of each of the resonances by measuring the spectral shift in response to changes in the refractive index of the surrounding medium. In addition, we reveal the sensing range of the different resonances through simulations involving a layer of deviating refractive index of increasing thickness. Interestingly, the resonances show very different responses, which we describe via the analysis of the near-field. This work contributes to the development of highly sensitive and selective BIC-based sensors that can be used for a wide range of applications.

© 2024 Optica Publishing Group under the terms of the [Optica Open Access Publishing Agreement](#)

1. Introduction

Optical sensors offer unique characteristics, such as precision, remote read-out, and immunity to electromagnetic interference. Optical refractive index sensors are particularly appealing because they do not require a label on the analyte to generate a signal. Instead, they use an optical transducer such as a plasmonic or photonic nanostructure that exhibits a resonance shift in response to a refractive-index change in the near-field of the transducer. Their label-free nature greatly simplifies their operation and as such they find applications in various research fields [1–6], ranging from environmental monitoring [7] to chemical characterization [8], and biosensing [9].

Label-free sensors can be broadly classified into two types: metal-based surface plasmon resonance (SPR) biosensors [10,11], and dielectric-based guided-mode resonance (GMR) biosensors [12,13]. In SPR sensors, a gold film is illuminated at a high angle through, e.g. a prism, leading to the excitation of a propagating surface plasmon polariton (SPP) that is sensitive to the refractive index in its evanescent field. This SPP creates a strongly localized near-field, albeit with a limited quality factor (Q) due to losses in the metal. Therefore, the merit figure (FoM) of SPR sensors (defined as the ratio between the refractive index sensitivity of a resonance and its full width at half maximum (FWHM)) is limited [14–16]. On the other hand, GMR-based sensors can support high-Q resonances by employing low-loss dielectric materials. However, the reduction in resonance linewidth is often accompanied by confinement of the electromagnetic field inside the structure [12], leading to a lower sensitivity to the surrounding refractive index.

Bound states in the continuum (BICs) have recently emerged as promising structures for sensing because they offer exceptional control over the resonance wavelength, Q-factor, and near-field confinement [5,17–24]. BICs arise in more complex periodic structures of scatterers and are defined as non-radiative modes that coexist with the continuum spectrum of radiating waves [25,26]. Two different types of BICs can be realized in periodic systems or metasurfaces: symmetry-protected BICs and accidental BICs [27,28]. Specifically, symmetry-protected BICs are optical modes that possess theoretically infinite Q-factors through their odd field symmetry that cannot couple with the even symmetric waves of the electromagnetic continuum. States that do not radiate cannot be detected in the far field, but the introduction of an asymmetry in the periodic structure allows a weak coupling with the radiation continuum, resulting in leaky resonances with high but finite Q-factors, called quasi-BICs [29].

By using quasi-BICs in metasurfaces, it is possible to achieve high-Q resonances without the drawback of material dispersion and absorption, as observed in SPR-based sensors. Additionally, the more localized electromagnetic field issue encountered in GMR-based sensors is avoided. These improvements make quasi-BICs a promising platform for high-performance sensing. In recent years, quasi-BICs have been intensively investigated for bio- [17,30–32], and bulk-refractive-index sensing [33–37], with sensitivities (S) ranging from 86.7 to 657 nm RIU⁻¹ and Figures of Merit (FoM) from 46 to 266 RIU⁻¹. Other potential advantages of quasi-BICs are the control of the tunability of their central wavelength, linewidth, and radiation pattern, which could be exploited to couple light in defined directions for interrogation in the visible with low-resolution and cheap spectrometers.

Works highlighting the differences between multiple quasi-BICs in the same structures are seldom [5,33,35]. This paper presents an all-dielectric multi-resonant metasurface supporting quasi-BIC resonances induced through various asymmetries [34]. In particular, we investigate the size- and position-detuning of a silicon periodic lattice of nanodisk dimers. We explore the fundamental differences between the resonances of our structure via electromagnetic field simulations, showing the magnetic and electric character of the different modes in the near-field region. In addition, we reveal that the resonances show vastly varying sensing characteristics in terms of sensitivity, Figure of Merit, and sensing range, which we explain via near-field studies. Finally, we show that the resonances exhibit a variation in robustness when exposed to refractive-index changes in the surrounding medium, indicating that some resonances are more sensitive to fabrication imperfections than others.

2. Metasurface design and fabrication

Our all-dielectric metasurface (Fig. 1) consists of a symmetry-broken rectangular lattice of silicon cylindrical nanodisk dimers on a SiO₂ substrate [38]. The designed metasurface was fabricated as follows: Polycrystalline Si thin films with a thickness of 90 nm were grown on a synthetic silica glass substrate by low-pressure chemical vapor deposition using SiH₄ gas as a source of Si. A resist (NEB22A2, Sumitomo) was cast on the Si film and exposed to electron-beam lithography, followed by the development to make nanodisk arrays of resist on the Si film. The Si film was vertically etched using a selective dry etching (Bosch process) with SF₆ and C₄F₈ gases, and the resist residue was etched away by dry oxygen etching. The fabricated area of the array covers 2 × 2 mm².

The optical modes of this metasurface have been discussed in detail in Ref. [38]. The C₂-symmetry of the array, responsible for the decoupling of the BIC from the radiation continuum, is broken through the size detuning between the two nanodisks of the Si dimer that form the unit cell. As shown in section 3, this symmetry breaking leads to a narrow resonance (quasi-BIC) at long wavelengths formed by the antiparallel in-plane electric dipole moments of the nanodisks. The displacement of the center of the nanodisks from a separation distance of $a_x/2$, with a_x the lattice period in the x -direction, to $a_x/2 - 2\Delta x$, leads to the evolution of a magnetic guided mode

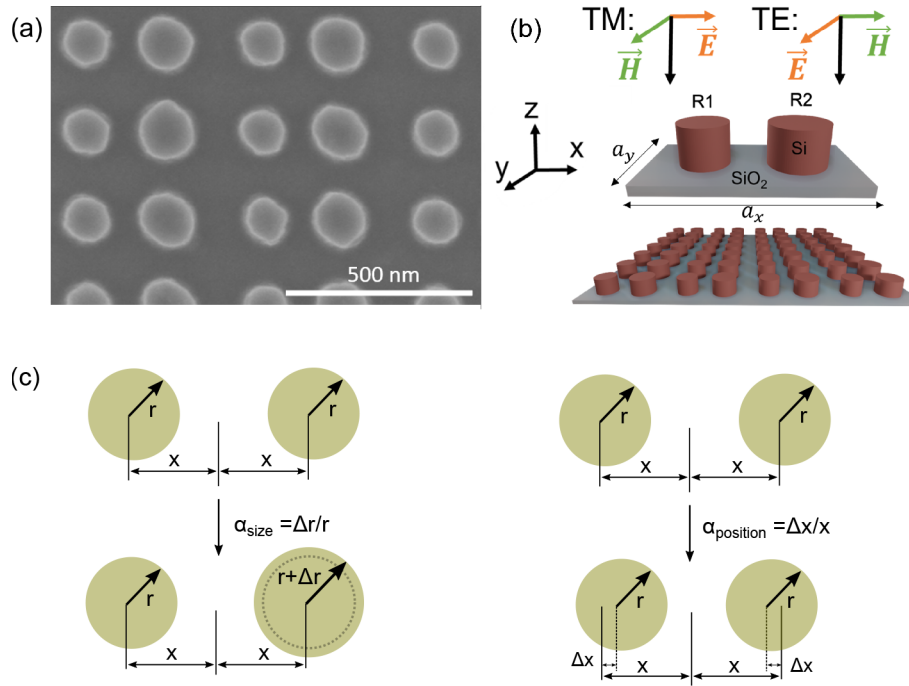


Fig. 1. (a) Scanning electron microscope image of the fabricated sample, and (b) schematic representation of a single unit cell and a larger area of size- and position-symmetry broken silicon dimer array on SiO_2 , including the definition of the polarization of the incident light with respect to the orientation of the particle array. (c) Schematics of different configurations of a unit cell of the metasurfaces, together with the corresponding asymmetry parameters α . The left panel shows cylindrical disks that provide symmetry breaking by increasing the radius of one of the disks, where the asymmetry parameter is given by $\alpha_{\text{size}} = \Delta r/r$. The right panel depicts cylindrical disks where both disks are shifted to the inside by a distance Δx . The asymmetry parameter is given by $\alpha_{\text{position}} = \Delta x/x$.

into a narrow bright mode at short wavelengths that we call the short-wavelength quasi-BIC. In section 3, we show that this mode results from the antiparallel oscillation of the out-of-plane magnetic dipoles in the nanodisks [38]. We have optimized the quality factor of the quasi-BIC resonances by tuning the asymmetry in the unit cell of the array and the distance between nanodisks. The dependence of the asymmetry on the quality factor was studied theoretically by Koshelev et al. [29], showing that the quality factor of quasi-BIC resonances is inversely proportional to the inverse square of the asymmetry parameter ($Q \propto 1/\alpha^2$). In the case of our size- and position-detuned nanodisks, the asymmetry parameters are defined as $\alpha_{\text{size}} = \Delta r/r$ and $\alpha_{\text{position}} = \Delta x/x$, where r and x denote the radius of the disk and the distance from the middle of the unit cell, respectively, while Δx and Δr reflect the amount of detuning of the respective parameters. We note that displacing the nanodisks does not break the C_2 -symmetry of the array, and the narrow short-wavelength quasi-BIC emerges from the coupling between the in-plane electric dipoles and the out-of-plane magnetic dipoles of the nanodisks [38]. Figure 1(c) depicts a schematic that indicates how the asymmetry parameters affect the dimensions of the particles and the array.

Our sensor operates in the visible range. However, the operating wavelength can be tuned by scaling the dimensions of the unit cell. After adjusting the dimensions and symmetry of the structure, the resulting array (see Fig. 1) consists of nanodisks ($r = 65 \text{ nm}$, $h = 90 \text{ nm}$) arranged

in a lattice of period $a_x = 469$ nm and $a_y = 235$ nm with asymmetry parameters $\alpha_{\text{size}} = 0.15$ and $\alpha_{\text{position}} = 0.1$.

3. Characterization of the quasi-BIC resonances

To characterize the samples, angle-dependent extinction measurements have been conducted and compared to simulations. The setup used for these measurements is illustrated in section S1 of Supplement 1. We measure the zeroth-order (forward) transmission spectrum by illuminating the sample with a collimated white light source. To realize a homogeneous medium covering the nanodisks, a 200 nm layer of 5% polyvinyl alcohol (with index $n = 1.48$) in water has been spin-coated on top of the surface. We calculate the optical extinction, defined as $Ext = 1 - T/T_0$, where T is the transmission through the array and T_0 is the transmission measured through a reference area, consisting of a substrate without disks but with the polyvinyl alcohol. The simulations are performed with COMSOL Multiphysics using a single unit cell with periodic conditions. For the substrate and Si refractive index, we employ data from Palik [39], and experimental data obtained from ellipsometry measurements (see Supplement 1 Fig. S2), respectively. The experimental and simulated extinction spectra as a function of the angle of incidence θ_{in} for TE-polarization are shown in Fig. 2, exhibiting excellent agreement.

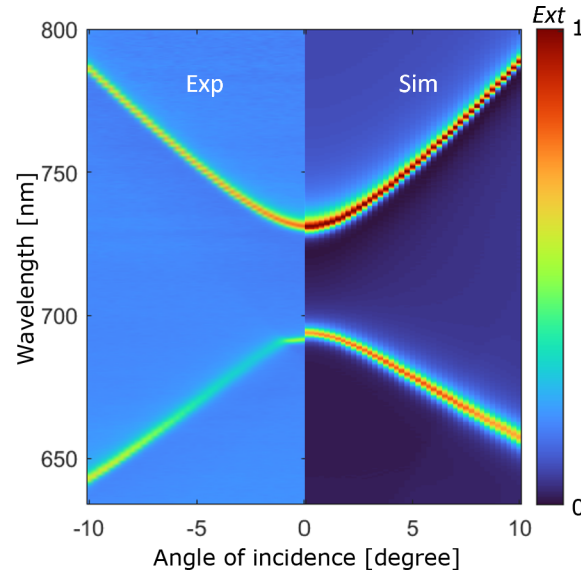


Fig. 2. Experimental (left) and simulated (right) extinction dispersion of a dimer nanodisk array embedded in a homogeneous medium ($n = 1.48$). The extinction spectra are plotted as a function of the incident angle for illumination of TE incident light. We vary the angle of incidence by rotating the sample in the xz -plane.

The metasurface of Si nanodisks shows two highly-dispersive narrow resonances, which correspond to quasi-BICs resulting from size and position detuning [38]. The dispersion follows the in-plane diffraction orders (Rayleigh anomalies), as defined by

$$\vec{k}_0 = \vec{k}_x(\theta_{\text{in}}) \pm \vec{G}(m_1, m_2) \quad (1)$$

where \vec{k}_0 is the wave vector of the in-plane diffracted orders, \vec{k}_x is the in-plane component of the wave vector of the incident light, and $\vec{G}(m_1, m_2) = m_1 \left(\frac{2\pi}{a_x}\right) \vec{x} + m_2 \left(\frac{2\pi}{a_y}\right) \vec{y}$ is the reciprocal lattice vector of the array, with m_1 and m_2 the orders of diffraction in the x - and y -directions. Using

Eq. (1) for $\vec{k}_x = 0$ (normal incidence) and considering that $|\vec{k}_x| = k_x = \frac{2\pi n}{\lambda} \sin\theta$, we find that the condition for the grating diffracted order in a lattice is met when $\lambda^{-1} = (an)^{-1} \sqrt{m_1^2 + m_2^2}$. For the lowest order, i.e., $(m_1 = \pm 1, m_2 = 0)$ or $(m_1 = 0, m_2 = \pm 1)$, $n = 1.48$ and $a_x = 469$ nm, we find that this condition is satisfied at $\lambda = 694$ nm, which is slightly below where the short-wavelength resonance appears in Fig. 2. The splitting between the resonances increases with increasing the angle of incidence, as also follows from Eq. (1).

To understand the origin of the two quasi-BIC resonances, we have performed a near-field numerical study, showing the local electric field profiles at different planes in the unit cell. Figure 3 shows the electric field distributions of these quasi-BICs in the xy - and yz -planes. In particular, Figs. 3(a),(c), show that the short-wavelength quasi-BIC mainly consists of an out-of-plane magnetic dipole moment (MD_z) (see the circulating displacement current in Fig. 3(a)). While Figs. 3(b),(d) illustrate the local electric-field distribution of the long-wavelength quasi-BIC, mainly showing an in-plane electric dipole moment (ED_y).

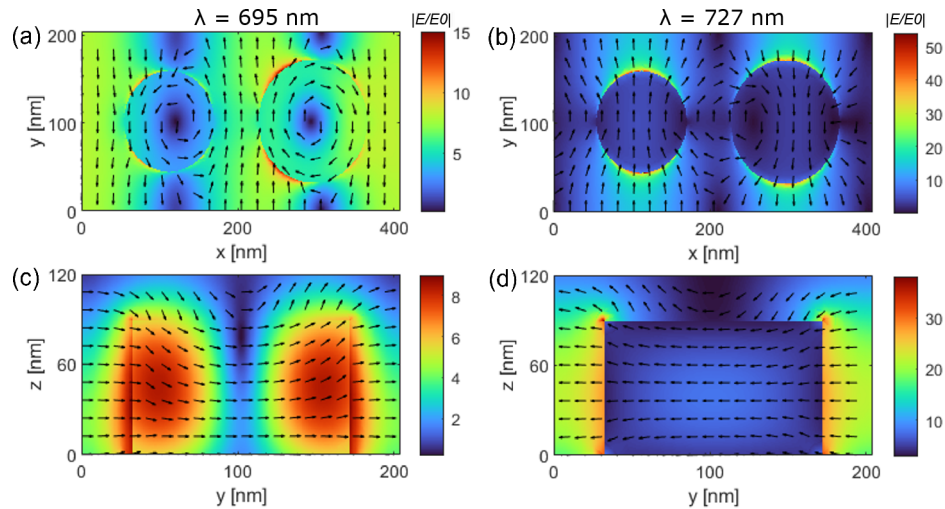


Fig. 3. Simulated electric-field enhancement $|E/E_0|$ for normal incidence in the xy -plane at the top surface of the nanodisks (a) (b), and in the yz -plane cutting through the larger particle (c)(d) for the short (a)(c) and long (b)(d) wavelength quasi-BICs at $\lambda = 695$ nm and 727 nm, respectively. The simulations use the same geometry as the fabricated sample discussed in section 2. The arrows represent the local electric field direction.

The main difference between the near-field images of the two quasi-BICs is that for the long-wavelength mode, there is much less field inside the volume near the surface of the particles (fundamentally due to the Maxwell equation boundary condition, with a jump in the normal electric field due to the index contrast), making it much more robust when exposed to surface imperfections. The short-wavelength quasi-BIC has a circulating electric field, so the continuity of the tangential field leads to similar amplitudes inside and outside of the disk. Notice also how the electric field intensity for the long-wavelength quasi-BIC (Fig. 3(b),(d)) is higher and more localized outside the disks, increasing its sensitivity to surface imperfections.

For completeness, the extinction spectra for TM polarization have also been simulated and measured, which is shown in Fig. S3 of Supplement 1. For this polarization, the two resonances are visible in simulation, but in measurements, they appear much weaker. This could be explained by the simulated near-field distributions shown in Fig. S4 of Supplement 1, indicating relatively larger fields inside the disk contours and an increased sensitivity to surface imperfections (visible in the SEM image Fig. 1(a)), which results in much weaker experimental extinction spectra.

4. Refractive index sensing

To demonstrate the sensing capabilities of the array of Si dimer nanodisks, bulk refractive index (RI) measurements have been performed. We vary the RI of the surrounding medium using RI-matching oils ($n=[1.4, 1.41, 1.42, 1.436, 1.47, 1.48, 1.50, 1.53, 1.55, 1.60]$) and measure the extinction spectra under normal incidence of a TE-polarized collimated white light beam. Spectra are measured using a confocal microscope connected to a spectrometer (Andor iDus DU420A).

Figures 4(a),(b) display the spectra of the short- and long-wavelength quasi-BICs, respectively, showing that an increase in RI of the surrounding medium results in a redshift of the resonant wavelength of both modes. The short-wavelength quasi-BIC shows a weaker extinction for refractive indexes of the matching oil deviating from the RI of the substrate ($n_{\text{SiO}_2} \approx 1.48$). The importance of a homogeneous medium for the robustness of resonances has been previously researched by Barnes et al. [40], where it was found that differences between the refractive indexes of the substrate and superstrate reduce the radiative coupling between the particles that lead to the collective modes of the array. This could explain the degradation of the extinction in Fig. 4(a) when we the refractive indexes become different. However, scattering simulations of the perfect unit cell do not reflect this behavior, showing consistent peaks over the whole measured RI range, indicating that the lack of robustness of the short-wavelength quasi-BIC must be due to an increased sensitivity to fabrication imperfections. This sensitivity can be qualified by determining the fraction of the modal energy that is located in a narrow zone at the outer diameter of the disks. Surface roughness can be modeled indirectly via extra losses in a zone near the surface [41], so the energy fraction at the surface is a good indicator of sensitivity to imperfections. We obtain an energy fraction in the outer layer of 35% for the short-wavelength quasi-BIC, versus a fraction of 10% for the long-wavelength quasi-BIC, again illustrating the different nature of the modes, which is clearly reflected in the profiles of Fig. 3. Section S4 of Supplement 1 explains in more detail how this simulation has been conducted, including figures showing the energy percentage in the outer layer as a function of wavelength (Fig. S5). In contrast, the long-wavelength resonance depicted in Fig. 4(b) shows a very robust behavior upon changing RI, with an average full width at half max of $FWHM = 2.15 \pm 0.3$ nm.

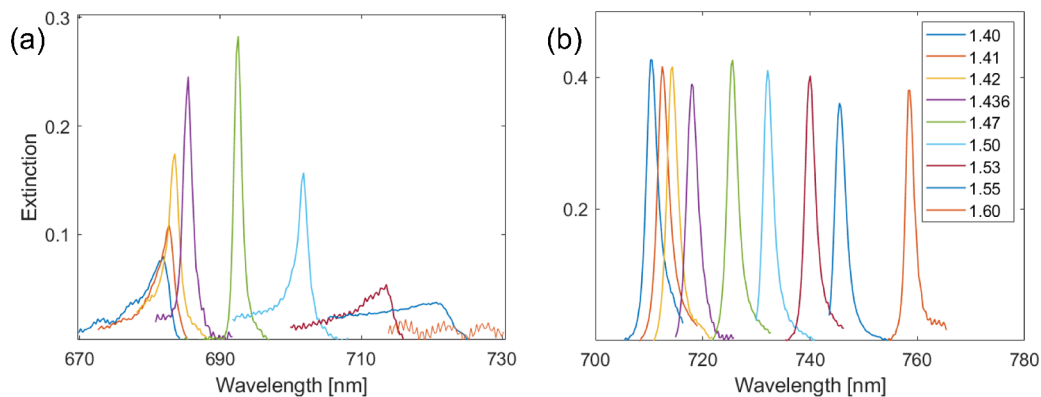


Fig. 4. Evolution as a function of the RI of the upper medium surrounding the array of dimer nanodisks of (a) short-wavelength quasi-BIC, and (b) long-wavelength quasi-BIC.

When we track the maxima of the extinction spectra as a function of the RI of the surrounding medium, we obtain Fig. 5 for both measurements (solid lines) and simulations (dashed lines). The measurements have been repeated 5 times on different areas of the particle array. The

measurements shown in Fig. 5 correspond to the mean value of these measurements, with the error bar given by the standard deviation.

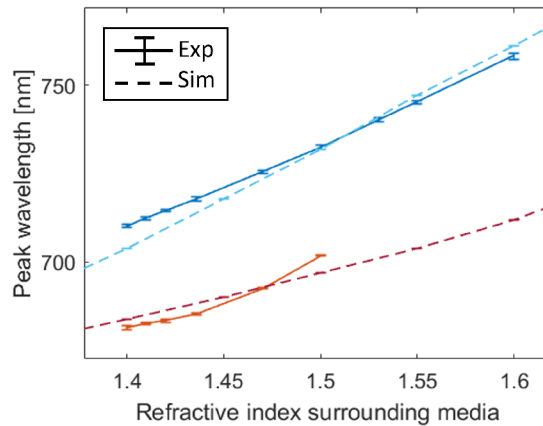


Fig. 5. Measured and simulated resonant wavelength as a function of the RI of the upper medium surrounding the array of Si dimer nanodisks.

Notice in Fig. 5 that for the short-wavelength quasi-BIC, we only include the data points up to $n = 1.5$, as the transmission spectra for $n > 1.5$ shows too weak extinction (see Fig. 4(a)). We can calculate the sensitivity of both modes to changes in RI of the surrounding medium with $S = \delta\lambda/\delta n$. The sensitivity is related to the distribution of the field within and outside the nanoparticles. In particular, when this field is distributed mainly in the surrounding medium, changes in refractive index can be detected more sensitively. Therefore, the long-wavelength mode has a higher sensitivity than the short-wavelength one because of its larger field enhancement in the surrounding medium of the nanoparticles, which leads to a better mode overlap with this medium as can be seen in Fig. 3. The short-wavelength mode shows a non-constant sensitivity in the experiments, with a nonlinear shift of the resonance with the refractive index. The sensitivity increases thus as we increase the RI. This non-linearity is also visible in the simulations, although it is much weaker and on a larger scale of RIs (not plotted in Fig. 5). This non-linearity can be explained via near-field simulations. We have computed the field intensity in regions in- and outside the particles as a function of RI, finding that for the short-wavelength quasi-BIC, the percentage of the total field energy located in the region outside of the nanoparticles rose from 30.6% for $n=1.4$ to 44.7% for $n=1.6$. This difference indicates that for an increase in RI, the sensor becomes more sensitive to external changes [22].

The simulation of the field intensity in regions in- and outside the particles has also been performed for the long-wavelength quasi-BIC, which shows a linear behavior in Fig. 5. The percentage of the total field energy located outside of the particles only slightly rises from 70.0% for $n=1.4$ to 72.1% for $n=1.6$, which reflects on the nearly constant slope of the long-wavelength quasi-BIC in Fig. 5. For this mode, we find an experimental sensitivity of $S_{\text{long,exp}} = 240 \pm 2$ nm/RIU and a simulated sensitivity of $S_{\text{long,sim}} = 277$ nm/RIU.

The long-wavelength quasi-BIC shows consistent extinction spectra (see Fig. 4(b)) over the whole RI range, which enables us to calculate the Figure of Merit (FoM), defined as $FoM = S/FWHM$. This FoM includes the sharp nature of resonances, and thus examines the effectiveness of a system to sensitively measure small wavelength shifts. Using the previously calculated $FWHM = 2.15 \pm 0.3$ nm and sensitivity ($S_{\text{long,exp}} = 240 \pm 2$ nm/RIU), we find $FoM = 111.6 \pm 0.14$. Typical sensors based on surface lattice resonances in nanoparticle arrays have FoM s in the range of 20-50 [42,43], indicating that quasi-BIC resonances can significantly improve this FoM . This improvement can be attributed to the larger field enhancement and

confinement to the surface of quasi-BICs compared to SLRs, as recently demonstrated in Ref. [44].

5. Biosensing simulations

To further investigate the sensing performance of our array of Si dimer nanodisks to local changes in RI, we simulate the sensitivity to a biomolecular layer attaching to the surface of the particles. Typically for biosensors, the surface of nanoparticles is functionalized through bio-active molecules dissolved in water that bind to target biomolecules; thereby creating a local change in RI in a layer around the surface of the particles. This process is simulated by increasing the thickness of a conformal layer of fixed RI, while we track the shift in resonant wavelength. In doing so, we obtain information about the resonance sensing range or how far away from the surface the resonances can sense RI changes. Figure 6 shows the shift in resonant wavelength for the short- and long-wavelength quasi-BICs as a function of the thickness of a dielectric conformal layer with $n = 1.5$, while the structure is submerged in water (dielectric of $n = 1.33$).

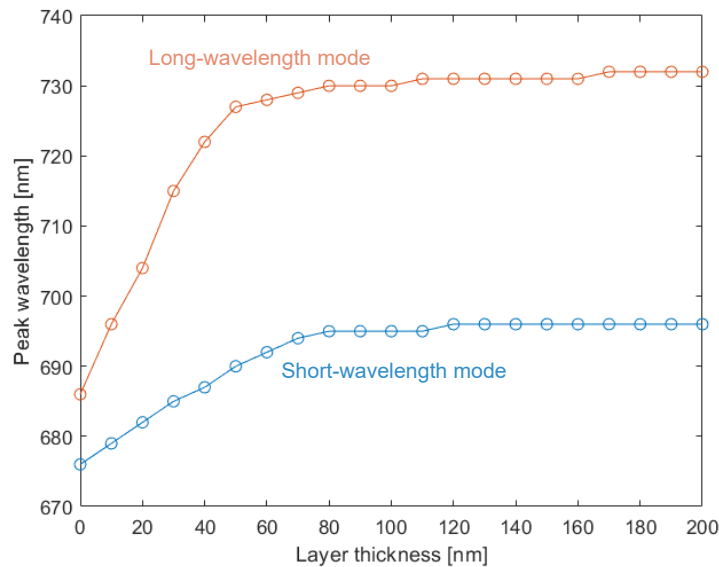


Fig. 6. Simulations of the resonant wavelength of quasi-BICs in arrays on Si dimer nanodisks as a function of a dielectric ($n = 1.5$) conformal layer thickness.

As a result of the increase in thickness of the conformal layer, the resonant wavelength of both modes redshifts. For small thickness changes, the resonant wavelength shifts with a large slope, but after a certain thickness, the shift saturates, and any increase in layer thickness will not result in a further shift. The thickness for which this occurs is defined as the saturation thickness, which is a measure of the sensing range of the resonance. The saturation thickness can be calculated by plotting two linear fittings, one tangential to the first part of the curve ($t < 20$ nm) and one tangential to the last part of the curve ($t > 180$ nm). The thickness where these linear fittings intersect is defined as the saturation thickness (Fig. S5 of Supplement 1 visualizes this method).

From Fig. 6, we notice that the long-wavelength quasi-BIC is characterized by a high initial sensitivity to changes in thickness of the conformal layer, which in the range of $0 < t < 40$ nm is calculated to be $S_{\text{long}} = 0.9 \text{ nm}/t[\text{nm}]$. The high sensitivity of this mode can be attributed to the high intensity of the electric fields in close vicinity of the surface of the nanoparticles, as depicted in Figs. 3(b),(d). However, after a thickness of $t_{\text{sat,long}} = 48$ nm, the shift saturates,

and an increase in layer thickness will only have a minor influence on the resonant wavelength, which indicates that for the long-wavelength quasi-BIC, there is a negligible amount of energy confined in the region $t > 40$ nm. The short saturation thickness can also be explained by the field distribution plots (Figs. 3(b),(d)), where it is visible that the high-intensity fields mainly exist in the xy -plane away from the particles, while in the z -direction the intensity of the field is negligible. Having a conformal layer thicker than ≈ 50 nm will result in the connection of the layers of different unit cells. After ≈ 80 nm, the unit cell is completely filled and any increase in layer thickness will effectively only result in a thicker layer in the z -direction. Therefore, it is expected for a resonance that has most of the high-intensity fields in the xy -plane (see Fig. 3(b),(d)), to have its shift saturated when we increase the thickness past ≈ 50 nm.

A similar but less drastic effect is seen for the short-wavelength quasi-BIC, which shows a lower initial sensitivity (also calculated in the range $0 < t < 40$ nm) of $S_{\text{short}} = 0.28$ nm/t[nm]. On the other hand, the shift does saturate later at $t_{\text{sat,short}} = 67$ nm. The lower sensitivity and larger saturation thickness can be attributed to the fact that fields in close proximity to the surface of the particles have lower values (see Fig. 3(a),(c)). However, these fields do extend further away from the particles, which results in a larger saturation thickness.

Interestingly, the different quasi-BICs show a very different behavior. Although the longer wavelength displays high sensitivity in the region close to the particles, it lacks sensing range. For the short-wavelength quasi-BIC, it is the other way around. Depending on the application, it is possible to optimize the structure for either of these properties.

6. Conclusion

Typical research on quasi-BIC sensing only discusses sensing properties such as FoM and sensitivity. Although these are important features of a sensor, there are more factors to consider. This paper provides a comprehensive comparison between two modes induced by different types of asymmetries in metasurfaces formed by Si nanodisk dimers. We show that depending on the near-field distribution of the quasi-BICs, they display vastly different properties that influence not only the sensitivity and FoM , but also the way they operate in real measurements and their sensing range. We demonstrate the sensing characteristics of both quasi-BICs via bulk RI measurements and verify the results with electric near-field simulations. Finally, we demonstrate with simulations how distant from the surface changes in the RI can be sensed. These simulations replicate the biosensing experiments.

Funding. Nederlandse Organisatie voor Wetenschappelijk Onderzoek (680-47-628, SCOPE (Vici)); HORIZON EUROPE European Research Council (864772, MultiSense (P.Z.)); Japan Society for the Promotion of Science (JPJSBP120239921).

Acknowledgments. We thank Sarojini Mahajan for help with the measurements. This project was financially supported by the Dutch Organization for Scientific Research (NWO) through the Gravitation grant “Research Centre for Integrated Nanophotonics” and the Innovational Research Activities Scheme (Vici project no. 680-47-628). It has also been supported by the Bilateral Joint Research Project (JPJSBP120239921) from Japan Society for the Promotion of Science and the European Research Council (ERC) under the European Union’s Horizon 2020 Research and Innovation Programme (grant agreement No. 864772, MultiSense (P.Z.)).

Disclosures. The authors declare no conflicts of interest.

Data availability. Data underlying the results presented in this paper are not publicly available at this time but may be obtained from the authors upon reasonable request.

Supplemental document. See [Supplement 1](#) for supporting content.

References

1. B. Špačková, P. Wrobel, M. Bocková, *et al.*, “Optical biosensors based on plasmonic nanostructures: A review,” *Proc. IEEE* **104**(12), 2380–2408 (2016).
2. M. Luo, Y. Zhou, X. Zhao, *et al.*, “Label-free bound-states-in-the-continuum biosensors,” *Biosensors* **12**(12), 1120 (2022).

3. S. Joseph, S. Pandey, S. Sarkar, *et al.*, “Bound states in the continuum in resonant nanostructures: an overview of engineered materials for tailored applications,” *Nanophotonics* **10**(17), 4175–4207 (2021).
4. A. Ndao, L. Hsu, W. Cai, *et al.*, “Differentiating and quantifying exosome secretion from a single cell using quasi-bound states in the continuum,” *Nanophotonics* **9**(5), 1081–1086 (2020).
5. C. Liu, Y. Bai, J. Zhou, *et al.*, “Refractive index sensing by asymmetric dielectric gratings with both bound states in the continuum and guided mode resonances,” *Opt. Express* **29**(26), 42978–42988 (2021).
6. J. Hu, H. Guan, X. Liu, *et al.*, “High-performance gas sensor with symmetry-protected quasi-bound states in the continuum,” *Opt. Express* **31**(22), 36228 (2023).
7. C.-W. Huang, C. Lin, M. K. Nguyen, *et al.*, “A review of biosensor for environmental monitoring: principle, application, and corresponding achievement of sustainable development goals,” *Bioengineered* **14**(1), 58–80 (2023).
8. M. S. Luchansky and R. C. Bailey, “High-q optical sensors for chemical and biological analysis,” *Anal. Chem.* **84**(2), 793–821 (2012).
9. H. Inan, M. Poyraz, F. Inci, *et al.*, “Photonic crystals: emerging biosensors and their promise for point-of-care applications,” *Chem. Soc. Rev.* **46**(2), 366–388 (2017).
10. Y. Xu, P. Bai, X. Zhou, *et al.*, “Optical refractive index sensors with plasmonic and photonic structures: Promising and inconvenient truth,” *Adv. Opt. Mater.* **7**(9), 1801433 (2019).
11. A. M. Shrivastav, U. Cvelbar, and I. Abdulhalim, “A comprehensive review on plasmonic-based biosensors used in viral diagnostics,” *Commun. Biol.* **4**(1), 70 (2021).
12. D. Conteduca, I. Barth, G. Pitruzzello, *et al.*, “Dielectric nanohole array metasurface for high-resolution near-field sensing and imaging,” *Nat. Commun.* **12**(1), 3293 (2021).
13. N. Bontempi, K. E. Chong, H. W. Orton, *et al.*, “Highly sensitive biosensors based on all-dielectric nanoresonators,” *Nanoscale* **9**(15), 4972–4980 (2017).
14. A. E. Cetin and H. Altug, “Fano resonant ring/disk plasmonic nanocavities on conducting substrates for advanced biosensing,” *ACS Nano* **6**(11), 9989–9995 (2012).
15. Q. Le-Van, E. Zoethout, E.-J. Geluk, *et al.*, “Enhanced quality factors of surface lattice resonances in plasmonic arrays of nanoparticles,” *Adv. Opt. Mater.* **7**(6), 1801451 (2019).
16. A. V. Kabashin, P. Evans, S. Pastkovsky, *et al.*, “Plasmonic nanorod metamaterials for biosensing,” *Nat. Mater.* **8**(11), 867–871 (2009).
17. F. Yesilkoy, E. R. Arvelo, Y. Jahani, *et al.*, “Ultrasensitive hyperspectral imaging and biodetection enabled by dielectric metasurfaces,” *Nat. Photonics* **13**(6), 390–396 (2019).
18. D. N. Maksimov, V. S. Gerasimov, S. Romano, *et al.*, “Refractive index sensing with optical bound states in the continuum,” *Opt. Express* **28**(26), 38907–38916 (2020).
19. Y. Liang, K. Koshelev, F. Zhang, *et al.*, “Bound states in the continuum in anisotropic plasmonic metasurfaces,” *Nano Lett.* **20**(9), 6351–6356 (2020). PMID: 32479094
20. S. Mesli, H. Yala, M. Hamidi, *et al.*, “High performance for refractive index sensors via symmetry-protected guided mode resonance,” *Opt. Express* **29**(14), 21199–21211 (2021).
21. X. Du, L. Xiong, X. Zhao, *et al.*, “Dual-band bound states in the continuum based on hybridization of surface lattice resonances,” *Nanophotonics* **11**(21), 4843–4853 (2022).
22. D. N. Maksimov, V. S. Gerasimov, A. A. Bogdanov, *et al.*, “Enhanced sensitivity of an all-dielectric refractive index sensor with an optical bound state in the continuum,” *Phys. Rev. A* **105**(3), 033518 (2022).
23. Z. Jing, W. Jiaxian, G. Lizhen, *et al.*, “High-sensitivity sensing in all-dielectric metasurface driven by quasi-bound states in the continuum,” *Nanomaterials* **13**(3), 505 (2023).
24. Y. Tang, Y. Liang, J. Yao, *et al.*, “Chiral bound states in the continuum in plasmonic metasurfaces,” *Laser Photonics Reviews* **17**(4), 2200597 (2023).
25. H. Hemmati and R. Magnusson, “Resonant dual-grating metamembranes supporting spectrally narrow bound states in the continuum,” *Adv. Opt. Mater.* **7**(20), 1900754 (2019).
26. F. Wu, J. Wu, Z. Guo, *et al.*, “Giant enhancement of the goos-hänchen shift assisted by quasibound states in the continuum,” *Phys. Rev. Appl.* **12**(1), 014028 (2019).
27. M. Sidorenko, O. Sergaeva, Z. Sadrieva, *et al.*, “Observation of an accidental bound state in the continuum in a chain of dielectric disks,” *Phys. Rev. Appl.* **15**(3), 034041 (2021).
28. C. W. Hsu, B. Zhen, A. D. Stone, *et al.*, “Bound states in the continuum,” *Nat. Rev. Mater.* **1**(9), 16048 (2016).
29. K. Koshelev, S. Lepeshov, M. Liu, *et al.*, “Asymmetric metasurfaces with high-Q resonances governed by bound states in the continuum,” *Phys. Rev. Lett.* **121**(19), 193903 (2018).
30. J. Wang, J. Kühne, T. Karamanos, *et al.*, “All-dielectric crescent metasurface sensor driven by bound states in the continuum,” *Adv. Funct. Mater.* **31**(46), 2104652 (2021).
31. A. Leitis, M. L. Tseng, A. John-Herpin, *et al.*, “Wafer-scale functional metasurfaces for mid-infrared photonics and biosensing,” *Adv. Mater.* **33**(43), 2102232 (2021).
32. C. Schiattarella, G. Sanità, B. G. Alulema, *et al.*, “High-q photonic aptasensor based on avoided crossing bound states in the continuum and trace detection of ochratoxin a,” *Biosens. Bioelectron.: X* **12**, 100262 (2022).
33. M. Luo, Y. Zhou, X. Zhao, *et al.*, “High-sensitivity optical sensors empowered by quasi-bound states in the continuum in a hybrid metal–dielectric metasurface,” *ACS Nano* **18**(8), 6477–6486 (2024).
34. H.-H. Hsiao, Y.-C. Hsu, A.-Y. Liu, *et al.*, “Ultrasensitive refractive index sensing based on the quasi-bound states in the continuum of all-dielectric metasurfaces,” *Adv. Opt. Mater.* **10**(19), 2200812 (2022).

35. K. Watanabe and M. Iwanaga, "Nanogap enhancement of the refractometric sensitivity at quasi-bound states in the continuum in all-dielectric metasurfaces," *Nanophotonics* **12**(1), 99–109 (2023).
36. Z. Wang, J. Sun, J. Li, *et al.*, "Customizing 2.5 d out-of-plane architectures for robust plasmonic bound-states-in-the-continuum metasurfaces," *Adv. Sci.* **10**(7), 2206236 (2023).
37. Y. Zhou, Z. Guo, X. Zhao, *et al.*, "Dual-quasi bound states in the continuum enabled plasmonic metasurfaces," *Adv. Opt. Mater.* **10**(19), 2200965 (2022).
38. S. Murai, D. R. Abujetas, L. Liu, *et al.*, "Engineering bound states in the continuum at telecom wavelengths with non-bravais lattices," *Laser Photonics Reviews* **16**(11), 2100661 (2022).
39. E. Palik and J. Love, "*Handbook of Optical Constants of Solids*, no. v. 3 in Academic Press handbook series (Elsevier Science, 1998).
40. B. Augu   and W. L. Barnes, "Collective resonances in gold nanoparticle arrays," *Phys. Rev. Lett.* **101**(14), 143902 (2008).
41. H. Yang, H. Liu, B. Song, *et al.*, "Effects of roughness and resonant-mode engineering in all-dielectric metasurfaces," *Nanophotonics* **9**(6), 1401–1410 (2020).
42. P. Offermans, M. C. Schaafsma, S. R. K. Rodriguez, *et al.*, "Universal scaling of the figure of merit of plasmonic sensors," *ACS Nano* **5**(6), 5151–5157 (2011).
43. G. Li, Y. Shen, G. Xiao, *et al.*, "Double-layered metal grating for high-performance refractive index sensing," *Opt. Express* **23**(7), 8995–9003 (2015).
44. S. ter Huurne, D. R. Abujetas, N. van Hoof, *et al.*, "Direct observation of lateral field confinement in symmetry-protected thz bound states in the continuum," *Adv. Opt. Mater.* **11**(6), 2202403 (2023).